International Journal of Heat and Mass Transfer 225 (2024) 125385

Contents lists available at ScienceDirect

International Journal of Heat and Mass Transfer

journal homepage: www.elsevier.com/locate/ijhmt

Degradation of the ZT thermoelectric figure of merit in silicon when nanostructuring: From bulk to nanowires

Martí Raya-Moreno [a,1], Riccardo Rurali [a], Xavier Cartoixà [b,*]

[a] Institut de Ciència de Materials de Barcelona, ICMAB–CSIC, Campus UAB, 08193, Bellaterra, Spain
[b] Departament d'Enginyeria Electrònica, Universitat Autònoma de Barcelona, Bellaterra, 08193, Barcelona, Spain

ARTICLE INFO

Keywords:
Thermoelectrics
Nanowires
Phonon drag
ZT
Coupled e-ph Boltzmann transport equation

ABSTRACT

Since the landmark paper by Hicks and Dresselhaus [Phys. Rev. B **47**, 16631(R) (1993)], there has been a general consensus that one-dimensional nanoscale conductors, i.e. nanowires, provide the long sought paradigm to implement the so-called phonon-glass electron-crystal material, which results in large improvements in the thermoelectric figure of merit *ZT*. Despite some encouraging—though isolated—experimental results, this idea has never been subjected to a rigorous scrutiny and the effect of the coupled dynamics of electrons and phonons has usually been oversimplified. To bypass these limitations, we have calculated the effective thermoelectric parameters for silicon nanowires (SiNWs) by iteratively solving the coupled electron-phonon Boltzmann transport equation (EPBTE) supplied with first-principles data. This allows for an unprecedented precision in determining the correct dependence of the thermoelectric parameters with system size; including, but not limited to, the figure of merit and its enhancement or degradation due to nanostructuring. Indeed, we demonstrate that the commonly used relaxation time approximation (RTA), or the uncoupled beyond the RTA (iterative) solution fail to describe the correct effect of nanostructuring on the thermoelectric properties and efficiency in SiNWs due to the strong contribution of phonon drag to the Seebeck coefficient, so that the use of fully coupled solution of the EPBTE is essential to obtain the correct effect of nanostructuring. Most importantly, we show that, contrarily to what commonly argued, resorting to NWs is not necessarily beneficial for *ZT*. Indeed, in a wide range of diameters nanostructuring diminishes the Seebeck coefficient faster than the decrease in thermal conductivity, due to the suppression of very long wavelength phonons responsible for the largest contribution to the phonon drag component of the Seebeck coefficient. This penalty to *ZT* can be mitigated if the NWs have a very rough surface, providing additional reduction to the thermal conductivity. Additionally, we demonstrate that our methodology provides improved data sets for an accurate determination of doping concentration in NWs through electrical-based inference and excellent agreement with the available experimental data.

1. Introduction

The growing interest in energy harvesting has led to the research for more efficient thermoelectric systems (i.e. systems that can convert thermal into electric energy) [1–5]; as they not only allow giving a practical use to recycle thermal waste but also generating energy for small wearable devices, thus removing the necessity of external batteries [6]. The efficiency of such systems is usually rated using the thermoelectric figure of merit, $ZT = \sigma S^2 T/\kappa$ [7], where σ, S, T and κ are the electrical conductivity, Seebeck coefficient, temperature, and thermal conductivity, respectively. Unfortunately, traditionally those systems offered quite a low efficiency (i.e. $ZT < 1$), therefore creating a need to enhance their energy conversion ratio [8,9]. This has brought into the spotlight the importance of phonon engineering or phononics, namely the use of nanostructuring to manipulate the vibrational properties of materials to increase ZT. Indeed, nanostructuring provides an effective way of reducing the lattice thermal conductivity without deteriorating electrical properties (i.e. obtaining a phonon-glass while keeping an electron-crystal) [7,6,10–12], thereby obtaining conversion ratios unachievable using more classical approaches, such as alloying [7]. A

* Corresponding author.
E-mail address: Xavier.Cartoixa@uab.es (X. Cartoixà).
[1] Currently at Institut für Physik und IRIS Adlershof, Humboldt-Universität zu Berlin, Newtonstr. 15, Berlin, 12489, Germany.

https://doi.org/10.1016/j.ijheatmasstransfer.2024.125385
Received 15 October 2023; Received in revised form 23 February 2024; Accepted 25 February 2024
Available online 6 March 2024

paradigmatic example of such an improvement due to nanostructuring can be found in Si nanowires (NWs) [13–18], which despite their simplicity have been found to offer, when heavily doped, a ZT 100 times larger than their bulk counterpart [19,20].

The quantities necessary for the computation of ZT can be readily obtained from the solution of the mesoscopic linearized Boltzmann Transport Equation for both electrons and phonons (EPBTE). The most common and simple approach is to decouple both systems, and then solve them using the so-called relaxation time approximation (RTA) [21,22], where it is assumed that each phonon mode and electronic state relaxes to equilibrium independently. However, more recent advances enable an iterative solution beyond that crude approximation—henceforth called *beyond*—for both phonons [23–25] and electrons [26–29]. Notwithstanding the improvement that the iterative solution offers over the RTA, the former still ignores the coupling (or drag terms) existing between both systems due to the electron-phonon interaction. Indeed, the inclusion of those terms becomes essential for a proper description of the thermoelectric properties, as for instance, they can greatly contribute to the Seebeck coefficient value in the NWs [30–33]. Consequently, the recent development of an iterative solution for the coupled system [34], i.e. one including the drag terms—henceforth referred as *dragged*—, has brought a step forward towards the more accurate computation of thermoelectric properties. Furthermore, informing the dragged EPBTE solvers with *ab initio* phonon and electron properties (energy, velocities, scattering rates,...) allows for an accurate description of these properties, including novel materials where simpler models to describe these are lacking [35,36]. Despite the utility of such an approach to accurately describe thermoelectric properties—recently made available to the community in the form of `elphbolt` package [35]—, its practical usage is currently limited to bulk, thus preventing its use for high-ZT systems such as nanostructured materials.

In this work, we extend the `elphbolt` package to compute the effective thermoelectric properties for nanosystems, specifically Si NWs, by iteratively solving the linearized EPBTE with the appropriate boundary conditions to correctly model the effect of perfectly diffusive physical boundaries, going for the first time a step beyond the most common approach based on the addition of a Casimir boundary scattering term through Matthiessen's rule [37,36,33]. We find that, contrary to the common thinking that any nanowire will enhance ZT because of the reduction in the thermal conductivity due to increased phonon boundary scattering [38–40], thick SiNWs have a ZT smaller than bulk Si, and that for *p*-doped (10^{18}–10^{19} cm^{-3}) smooth SiNWs one must go to small NW diameters ($\lesssim 60$ nm) in order to observe the enhancement. Additionally, while we do not find enhancement for *n*-doped (10^{18} cm^{-3}) smooth NWs at any diameter, it must be pointed out that our results do not take into account effects such as the elastic softening, which has been shown to strongly suppress the thermal conductivity in ultrathin Si nanotubes [41] and nanoribbons [42], and might restore the beneficial role of diameter reduction for ZT in ultra-scaled SiNWs—of course, the positive contribution would also be there for *p*-doped NWs. Also, there have been previous reports where, in ultra-scaled SiNWs of 3-12 nm, electronic confinement had a detrimental effect on the ZT of the SiNWs [43,44] but, as we will show, the reduction in ZT we observe takes place for SiNWs of 100 s of nm, and is due to the initial quenching of the phonon drag contribution to the Seebeck coefficient.

2. Results

2.1. Casimir-Matthiessen's approach vs "suppressed" treatment of the boundary scattering

Quantum, dielectric, and phonon confinement alter the electronic and thermal properties of NWs [45]. However, such confinement effects in Si are important only for diameters of at most 10 nm [46,45] and thus can be normally disregarded in NWs routinely grown and used in thermoelectric devices, whose diameters are typically of the order of 50-150 nm (see e.g. Ref. [15]). Confinement effects aside, the most prominent, distinctive feature of a NW, compared to the bulk, is electron and phonon boundary scattering. For this reason, the way boundary scattering is computed is crucial when it comes to the predictive power of calculations of the thermoelectric properties.

As detailed in the Methods section below, the widespread Casimir-Matthiessen (CM)-based approach to take into account size effects within the framework of the homogeneous PBTE suffers, in principle, from several theoretical shortcomings. For instance, it incorrectly affects carriers propagating along the growth direction in the case of NW, not only through the interaction with non-parallel modes—i.e. those affected by surface scattering—but directly. A more elaborated approach based on the initial work by Chambers [47] for electrons and later extended to phonons by Li [24,48] derives directly from averaging the non-homogeneous PBTE, and thus does not suffer from that and other flaws. In fact, Mingo et al. [49] have not only proven differences between both approaches but also the breakdown of the former rule in nanoribbons. Further details on both approaches (theory, limitations,...) can be found in Section 4.1.

Consequently, it is interesting to compare the results of CM with our methodology for the computation of effective thermoelectric quantities over a wider range of limiting sizes (i.e. radii) to investigate if such flaws translate to any physical incongruency with our approach, as this latter should in principle provide a more exact and physically grounded treatment of boundary effects, excluding surface states, donor/acceptor deactivation due to dielectric mismatch, surface-induced elastic softening and/or quantization effects.

In Fig. 1, we can see the different effective thermoelectric quantities—phonon and electronic (at zero field) thermal conductivity, Seebeck coefficient, electrical conductivity, the phonon (α_{ph}) and electronic (α_{el}) thermal response to an electric field—at 300 K for Si NWs with a B-doping of 1×10^{18} cm^{-3} computed with our approach and those obtained through the use of the CM one. There is a good agreement of suppressed- and CM-computed thermoelectric properties for large radii—i.e. relative differences lower than 5%, which is an acceptable experimental error for thermal conductivity [50]—. On the other hand, for thin NWs (R <100 nm) the relative error for all quantities except the Seebeck coefficient is larger. We note that for the thinnest radii under the scope of this work there is an indication that the phonon thermal response to an electric field (α_{ph}) might change sign; in other words, an opposite effect of the drag of electrons on phonons under the action of a homogeneous electric field. This effect might be larger in other materials, thus deserving further investigation.

Such a disagreement can be considered of little importance in our case, as the total thermal response to an electric field is dominated by the electronic component at small radii, which does not suffer from such qualitative discrepancy. On the other hand, this disagreement might be more appreciable in the description of the Peltier effect for the thinnest NWs, given a phonon dominance of the response.

Finally, we also point out that the values we obtain for the bulk (B-doped, 10^{18} cm$^{/3}$) electrical conductivity σ (30 S/cm) and phonon thermal conductivity κ_{ph} (126 W/m·K) are in excellent agreement with their respective experimental (B-doped, 1.8×10^{18} cm$^{/3}$) [51] counterparts of 31 S/cm and 124 W/m·K. On the other hand, the calculations slightly overestimate the Seebeck coefficient S, obtaining 960 μV/K against the measurement [51] of 600 μV/K. Notwithstanding this, it should be noted that Sen *et al.* computed [33] and Geballe and Hull measured [52] an S close to 1000 μV/K for B-doping at 10^{18} cm^{-3} (sample 141), but that value seems to be quite high when compared to more recent measurements [53].

2.2. Size effect on the thermoelectric effective magnitudes

Fig. 2 displays the main result of our study: the dependence of the thermoelectric efficiency ZT of a Si NW as function of its radius. Sur-

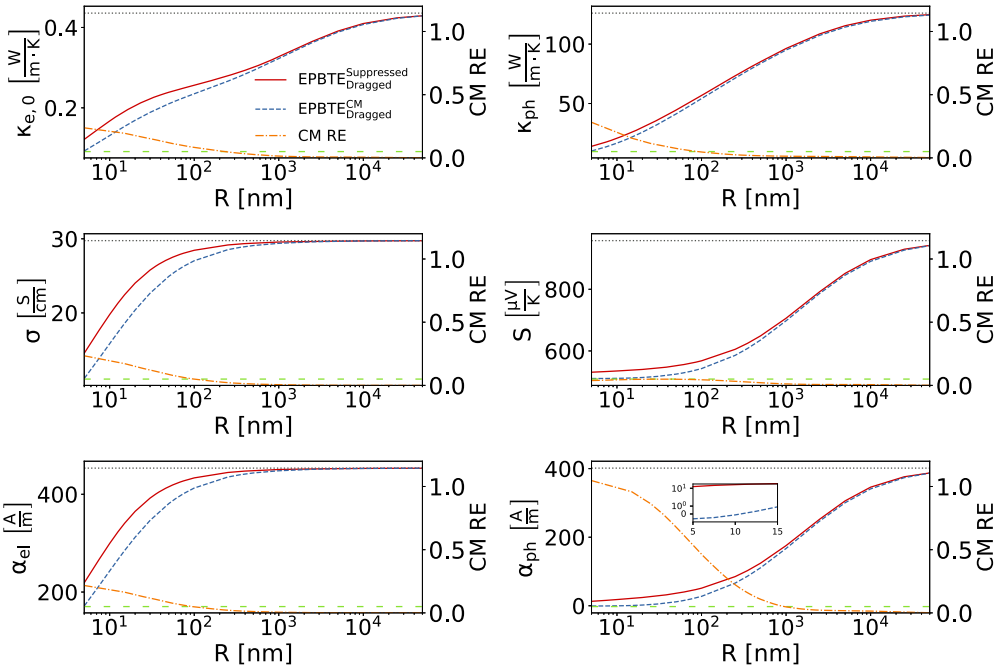

Fig. 1. Left-axis: Electronic (at zero field; $\kappa_{el,0}$) and phonon (κ_{ph}) thermal conductivity, electrical conductivity, Seebeck coefficient, the electronic (α_{el}) and phonon (α_{ph}) thermal response to an electric field as a function of NW radius at 300 K and acceptor concentration (B) of 1.0×10^{18} cm^{-3} obtained through the suppressed dragged EPBTE (red solid) and dragged EPBTE with CM (blue dashed); bulk values (gray dotted) are given as reference. Right-axis: Relative error of CM with respect to suppressed solution (orange dot-dash) as function of NW radii; we indicate the 5% relative error as reference (green loosely dashed). Inset: Zoom at small radii for α_{ph}. (For interpretation of the colors in the figure(s), the reader is referred to the web version of this article.)

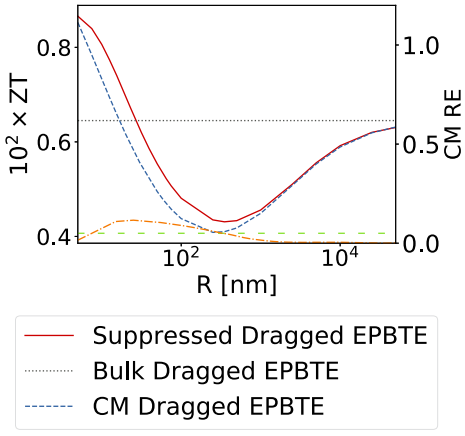

Fig. 2. Left-axis: Thermoelectric figure of merit as a function of NW radius at 300 K and acceptor concentration (B) of 1.0×10^{18} cm^{-3} obtained through the suppressed dragged EPBTE (red solid) and dragged EPBTE with CM (blue dashed); bulk values (gray dotted) are given as reference. Right-axis: Relative error of CM with respect to suppressed solution (orange dot-dash) as function of NW radii; we indicate the 5% relative error as reference (green loosely dashed).

prisingly, we found that, contrarily to what commonly argued, once drag effects are included (cf. Fig. 3), downscaling the NW diameter does not necessarily result in an increased ZT. Indeed, when one starts to reduce the thickness of the NW ZT at first *decreases*. Reducing the radius of the NW translates into an increase of ZT only for values smaller that 200-300 nm, where the curve exhibits a minimum. Nevertheless, it is only for radii smaller than $\sim$ 30 nm that nanostructuring pays off and yields ZTs larger than the bulk values. This is a very important result because Si NWs that are normally integrated in thermoelectric modules have typically larger diameters than this threshold value [13,15,11,12]. Therefore, while the one-dimensional nature of NWs can be beneficial for other reasons, the quest of a large thermoelectric figure of merit *per se* does not justify nanostructuring in smooth crystalline NWs, unless ultrascaled radii can be achieved (see e.g. Refs. [19,20], though in those cases other factors such as extremely rough surfaces are believed to play a role as well).

We find it also interesting to investigate the evolution of the predicted thermoelectric properties and the figure of merit of NWs as the rigor in the treatment (and the computational cost) is reduced, in the sequence *Suppressed dragged* → *Suppressed uncoupled Beyond-RTA* → *Suppressed uncoupled RTA*.

In Figs. 3 and 4 we present several effective thermoelectric properties as a function of the radius for *p*-type B-doped and *n*-type P-doped ⟨111⟩ SiNWs, with a doping concentration of 1.0×10^{18} cm^{-3}. Common to all cases, we observe that both RTA and beyond provide always lower values (in absolute value) than the dragged solution for the thermoelectric properties at all radii. Remarkably here is the Seebeck coefficient, which greatly differs in its behavior with radii decrease between the dragged and the other approaches, which translates into the $ZT(R)$ minimum present in the dragged solution, which is also qualitatively different from its non-dragged counterparts. The dependence of S on the NW radius is rooted in the fact that phonon distribution can keep its inertia longer than the electronic one and is thus more affected by boundary effects, so that its phonon (dragged) component is more sensitive to size than the electronic (diffusive) component.

This behavior is well captured by Fig. 5, which shows that while the electronic component is almost unaffected by size effects, the phonon contribution to S—which amounts to 40-45% of the total value of S, see right panel in Fig. 5—is highly suppressed by boundaries up to middle range radius values. In other words, for small radii the phonon distribution is highly damped by boundaries reducing its drag capacity over the less-damped electronic distribution—this translates into a similar slope of RTA, beyond and dragged for small radii; whereas, for higher radii, the phonon distribution becomes less damped and starts contributing to the Seebeck coefficient, originating the change of slope of the dragged case. Indeed, the $S_{ph}^{eff}(R)/S_{ph}^{bulk}$ results are in line with those of Zhou et al. [39] for the cumulative S_{ph} with the mean free path (see Figure 2B of

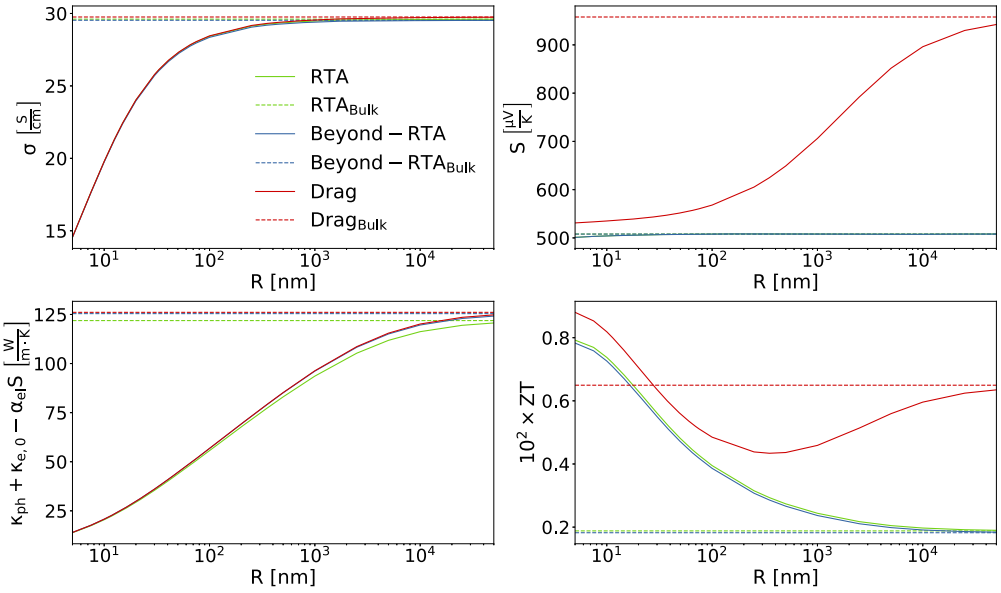

Fig. 3. Electrical conductivity, Seebeck coefficient, total thermal conductivity at zero electric current, and figure of merit as function of NW radius at 300 K and an acceptor concentration (B) of 1.0×10^{18} cm^{-3} for several approaches to collision operator; namely, RTA (green), uncoupled beyond the RTA (blue), and dragged (red). Bulk values (dashed) are given as reference.

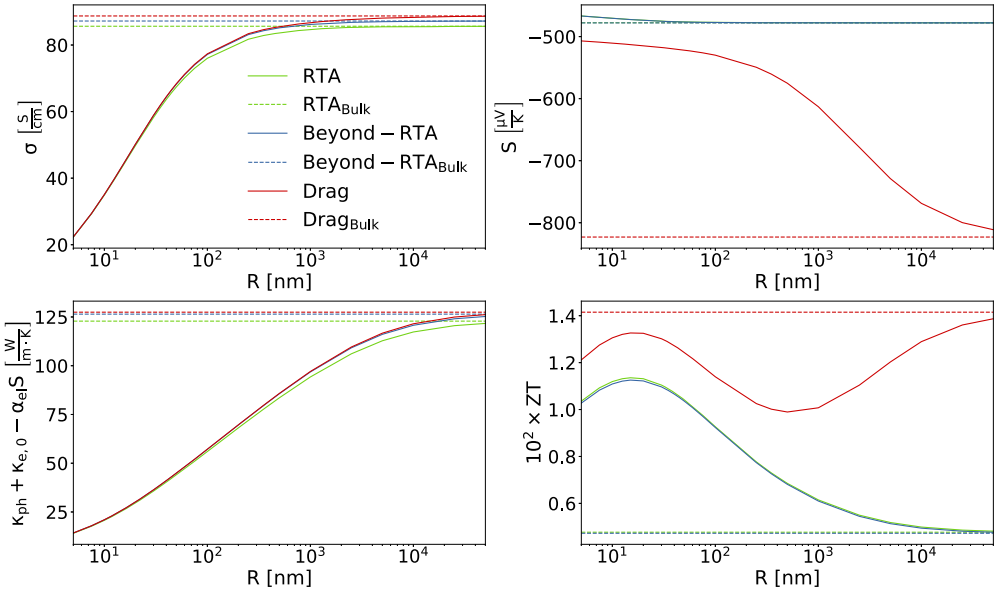

Fig. 4. Electrical conductivity, Seebeck coefficient, total thermal conductivity at zero electric current, and figure of merit as function of NW radius at 300 K and a donor concentration (P) of 1.0×10^{18} cm^{-3} for several approaches to collision operator; namely, RTA (green), uncoupled beyond the RTA (blue), and dragged (red). Bulk values (dashed) are given as reference.

Ref. [39]) though with a smoother behavior, typical of the suppressed quantities in comparison with the mean free path cumulative ones (see Figure 2 of Ref. [24]), thus further substantiating the great suppression caused by boundaries to the phonon drag.

Once again we stress that the main role of the drag effect is that—contrary to the other simplified approaches that provide always an improvement of the ZT for all radii—there is a wide diameter range where nanostructuring, rather than enhancing thermoelectric efficiency, deteriorates it. In this sense the case of smooth *n*-type NWs, for which no radius would provide an enhancement of the thermoelectric efficiency and the ZT of bulk would always be larger, is paradigmatic. However, it must be pointed out that our calculations assume bulk dispersions for electron and phonon bands and thus, as previously mentioned, do not take into account surface effects such as the elastic softening, which has been shown to strongly suppress the thermal conductivity beyond the Casimir limit in ultrathin Si nanotubes [41] and nanoribbons [42], and might restore ZT to above-bulk values in ultra-scaled SiNWs.

To summarize, as the SiNW radius is decreased, the sequence of the evolution of the magnitudes entering ZT is the following: $S_{ph}^{eff} \downarrow (ZT \downarrow) \rightarrow \kappa_{ph} \downarrow (ZT \uparrow) \rightarrow \sigma \downarrow (ZT \downarrow)$, explaining the behavior of ZT. For the *n*-type 1.0×10^{18} cm^{-3} SiNWs, Fig. 4 shows how the stronger reduction in σ causes their ZT value never to go above the bulk values within our treatment.

Building on findings, we can now determine the region where nanostructuring results in an enhancement of the thermoelectric efficiency. In Fig. 6 we depict the thermoelectric figure of merit and the power factor as a function of both radius and doping concentration for a *p*-type Si

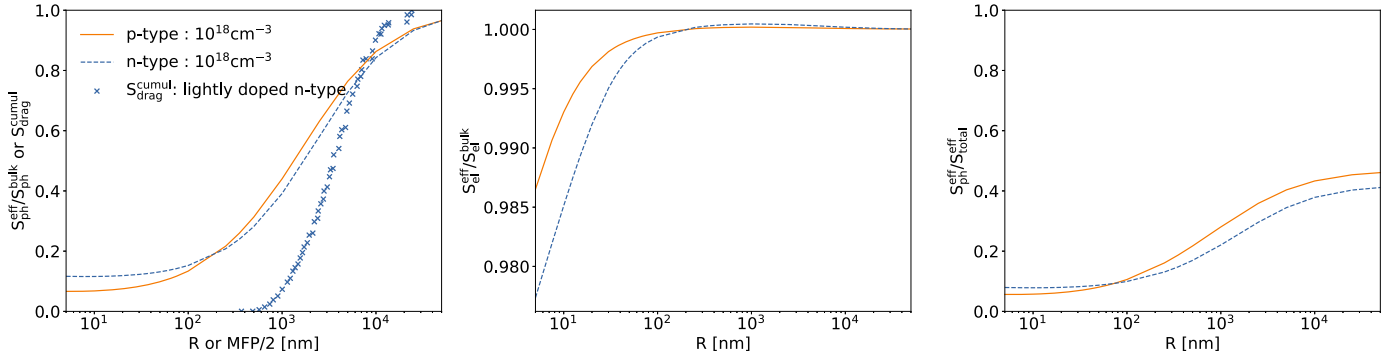

Fig. 5. Left: Ratio between the effective phonon component of the total Seebeck coefficient with respect to its bulk value as a function of the NW radius. Blue crosses indicate the cumulative contribution to $S_{\mathrm{ph}}^{\mathrm{drag}}$ as a function of half of the MFP of the corresponding phonons (data from Ref. [39]). Middle: Ratio between the effective electron component of the total Seebeck coefficient with respect to its bulk value as a function of the NW radius. Right: Ratio between the drag (phonon) component and the total Seebeck coefficient for different radii.

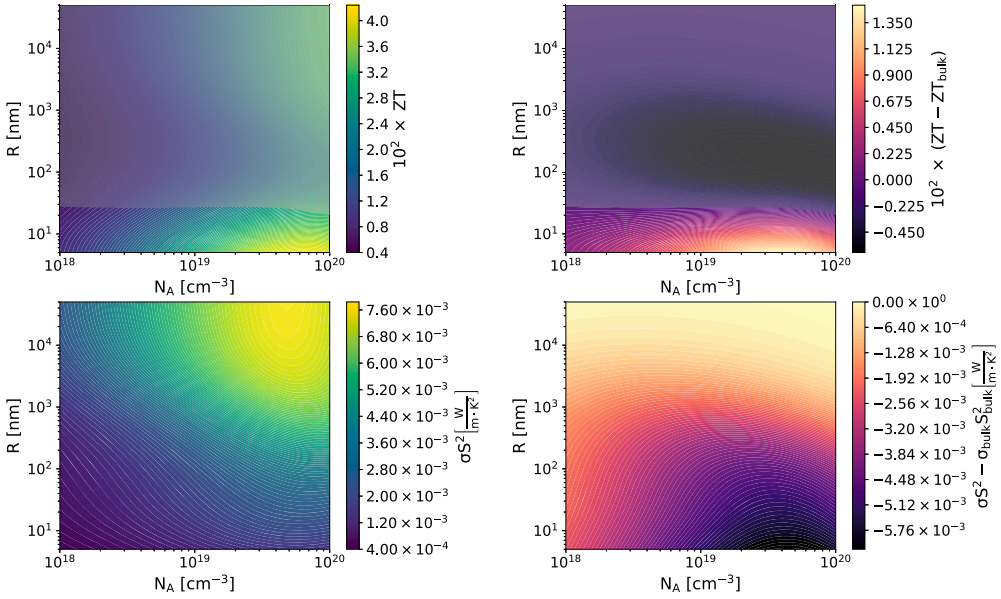

Fig. 6. Top-left: Figure of merit as a function of the radius and the acceptor concentration (B) for Si NWs at 300 K. Whitish area indicate ZT values lower than bulk at given doping concentration. Top-right: Difference between the NW and the bulk figure of merit as a function of the NW radius and the acceptor concentration (B) for Si NWs at 300 K. Whitish area indicate ZT values lower than bulk at given doping concentration. Bottom-left: Power factor as a function of the radius and the acceptor concentration (B) for Si NWs at 300 K. Bottom-right: Difference between the NW and the bulk power factor as a function of the NW radius and the acceptor concentration (B) for Si NWs at 300 K.

NW: this plot provides the guidelines to follow when synthesizing a Si NW for thermoelectric applications and, conversely, indicates the fabrication parameters to be avoided. Yet, we recall that our calculations should be taken as a limiting case, i.e. perfectly diffusive infinite NWs, and that increased surface roughness will improve the behavior of ZT.

2.3. Assessment of suppressed EPBTE for the prediction of effective thermoelectric quantities in Si NWs against experiments

We now assess the accuracy of our approach by comparing with the available experimental results of similar systems, that is extremely long NWs (i.e. with a length much longer than any RTA mean free path) with rough boundaries. To detail, we compare the results obtained with our methodology within the framework of the dragged collision operator, to the experimental values of Gadea et al. [11] (see Table 1); i.e. Si NWs with radii ranging 45-50 nm and B-doping of (2.0-5.0)×10^{19}cm^{-3}. Before proceeding with the comparison it is worth noting that the experimental NWs of Ref. [11] have an extremely rough surface. This would severely hinder the phonon distribution [54,55], and to a lesser extent the electronic one as this same rough shell partially shields the NW core from possible surface charges [56,57].

Indeed, while we observe a very good agreement for the electric conductivity, the obtained thermal conductivity within both approaches is higher than the experimental result; however, it is in line with experimental data for NWs with smoother surfaces [11,12]. As for the Seebeck coefficient, we observe similar predictions of the suppressed and CM methods, as expected, as the divergence is mostly contained in the non-dominant (i.e. ~8-11% of S) drag or phononic contribution to the Seebeck coefficient. Furthermore, our results for σ agree with those of Ref. [11], assuming a doping in the low end of the range extracted from σ quoted in that work—i.e. (2.0-3.0)×10^{19}cm^{-3}—. The doping range estimated in Ref. [11] from the S measurements is (2.0-5.0)×10^{19}cm^{-3}, and the measured S agrees with our prediction at 5.0×10^{19}cm^{-3}. This further substantiates the accuracy of our results, and also proves our calculations useful as a method to accurately determine the doping concentration in nanosystems taking into account boundary scattering; an improvement over other doping-determination methodologies which are solely based on bulk quantities [58,59]. Additionally, we also com-

Table 1
Calculated thermal conductivity (κ), electrical conductivity (σ), Seebeck coefficient (S) and thermoelectric figure of merit (ZT) at 300 K, for NWs of radii ranging 45-50 nm and B-dopings of 2.0×10^{19} and 5.0×10^{19} cm^{-3} using the suppressed dragged EPBTE and dragged EPBTE with Matthiessen's plus a Casimir scattering term (CM) to model the NW boundary effect. Results from Ref. [11] are provided as reference.

	N_A [cm^{-3}]	κ [W/m·K]	σ [S/cm]	S [μV/K]	$ZT\times10^2$
Experimental	2.00×10^{19} - 5.00×10^{19}	18.3±4.6 (13-25†)	270 (247-290†)	207±19	1.4-2.5†
Suppressed dragged EPBTE‡	2.00×10^{19}	39.8-41.5	304-306	289-290	1.9-1.9
	5.00×10^{19}	37.8-39.4	684-687	210-212	2.4-2.3
CM dragged EPBTE‡	2.00×10^{19}	38.2-40.0	288-291	282-284	1.8-1.8
	5.00×10^{19}	36.6-38.3	651-657	208-209	2.3-2.3

† These values correspond to the minimum and the maximum of the value for the given temperature of all measurements, including errors.
‡ These results correspond to the values for NWs of radius 45 (left) and 50 (right) nm.

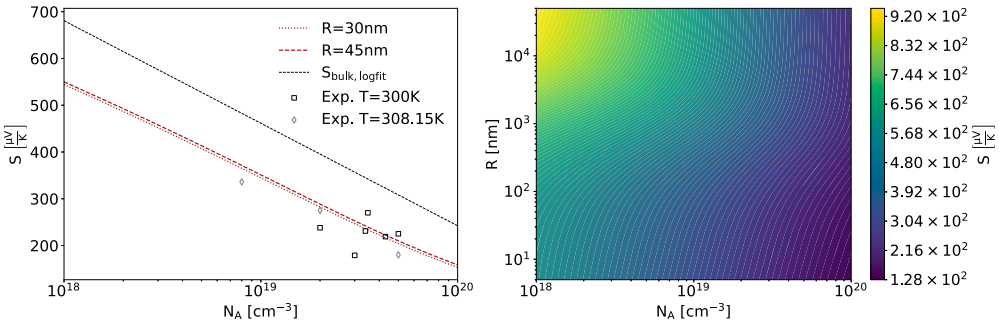

Fig. 7. Left: Seebeck coefficient as function of doping for B-doped NW of radius 30 (red dotted) and 45 (red dashed)nm at 300 K, and the associated bulk value obtained using logarithmic fitting of Ref. [53] (dashed black line). Black (gray) squares (diamonds) provide experimental values for NWs of similar characteristics at 300 K(308.15 K) [31,11,61,12] as reference. Right: Dragged Seebeck coefficient as a function of B-doping and NW radius at 300 K.

pare the results of our methodology against the experimental data of Ref. [12] for extremely rough Si NWs (see Table 2), obtaining a similar agreement level than in the former case.

Finally, we also provide the results using the classical CM approach to model boundary effects for the same case (see Table. 1), obtaining similar values for thermoelectric properties as with the suppressed model. These results agree with the previous discussion of Fig. 1 and 2, where we concluded that CM approach predicts essentially the same behavior as the more rigorous suppressed framework for the studied Si NWs with $R \gtrsim 30$ nm.

2.4. Doping concentration and Seebeck coefficient

Accurately determining the doping concentration of nanowires presents a significant challenge from an experimental standpoint. Whilst secondary ion mass spectrometry provides the most accurate measurement for dopant concentrations [31], this is not only an expensive technique, but it also degrades the sample. Consequently, electrical-based inferences are usually preferred, despite all their associated problems about their reliability [57,31]. This type of electrical determination involves comparing the obtained results with bulk-experimental data [60] and/or bulk-based theoretical fitting models (i.e., models with size-independent thermoelectric properties) [58,59,57]; see for instance Refs. [11] and [12]. However, in view of our simulations (see Fig. 1-4), it becomes challenging to justify the use of bulk values and/or bulk-based models to determine the doping of NWs since these values differ significantly from those found in NWs.

While the extension of simple theoretical models to account for finite-size effects can be considered, in light of our results any considered modification must accurately model both boundary effects and drag simultaneously. Therefore, we provide the Seebeck coefficient computed using the suppressed EPBTE as a function of doping for B-doped Si NWs, for several doping levels and radii in Fig. 7 left. The comparison against bulk experimental fittings using logarithmic fitting of Ref. [62,53]—a common methodology used, for instance, in Refs. [11,12]—reveals that our method provides significantly lower values of S than those expected for bulk Si, yielding results more in line with experimental results [11,12], i.e. a Seebeck coefficient between 402-103 μV K^{-1}. Moreover, Sojo et al. [12] suggest that the origin of these discrepancies is to be found in the interplay of phonon drag and boundary effects; something that is, indeed, proven and properly captured by our approach. Consequently, our results are expected to provide an improved dataset for the inference of doping concentration in B-doped Si NWs, including an improved logarithmic fitting formula including the NW radius R:

$$\mathrm{S}(\mathrm{N_A},\mathrm{R}) = \mathrm{a(R)}\ln(\mathrm{N_A}) + \mathrm{b(R)}, \tag{1}$$

$$\mathrm{a(R)} = \frac{-75.7714}{1+\mathrm{e}^{-1.1640\ln(\mathrm{R})+8.9839}} - 86.7513, \tag{2}$$

$$\mathrm{b(R)} = \frac{3586.7}{1+\mathrm{e}^{-1.1248\ln(\mathrm{R})+8.6242}} + 4133.6, \tag{3}$$

where B-doping concentration ($\mathrm{N_A}$) is given in cm^{-3}, radius (R) in nm, and S in μV K^{-1}.

Interestingly, the use of the doping concentrations from the inversion of Eqs. (1)-(3) from measured S and R instead of the bulk-fitted ones, considerably improves the agreement between the computed properties and the experimental ones (see interpolated properties in Table 3). In fact, this showcases the utility of our methodology for the systematic generation of accurate data sets for an improved determination of doping concentration in NWs for any material.

Table 2
Calculated thermal conductivity (κ), electrical conductivity (σ), Seebeck coefficient (S) and thermoelectric figure of merit (ZT) at 300 K, for NWs of radii ranging 30-45 nm and different B-dopings using the suppressed dragged EPBTE. Results from Ref. [12] are provided as a reference.

	N_A $[\mathrm{cm}^{-3}]$	κ $\left[\frac{\mathrm{W}}{\mathrm{m\cdot K}}\right]$	σ $\left[\frac{\mathrm{S}}{\mathrm{cm}}\right]$	S $\left[\frac{\mu\mathrm{V}}{\mathrm{K}}\right]$	$ZT\times10^2$
Experimental†	1.0×10^{19}	17.2±1.4	200	331	4.0
	5.0×10^{19}	17.2±1.4	425	225.1	3.0
Suppressed dragged EPBTE†	1.0×10^{19}	34.3-40.8	161-166	345-351	1.7-1.5
	5.0×10^{19}	32.0-37.8	668-684	204-210	2.6-2.4

† These results correspond to the values for NWs of radius 30 (left) and 45 (right) nm, with a B-doping of 1.0×10^{19} cm^{-3} (top) and 5.0×10^{19} cm^{-3} (bottom).

Table 3
Interpolated thermal conductivity (κ), electrical conductivity (σ), Seebeck coefficient (S) and thermoelectric figure of merit (ZT) at 300 K, for NWs with B-doping concentration computed using the experimental Seebeck coefficient by inversion of Eqs. (1)-(3) using experimental obtained radius limits, i.e. 30 and 45 nm. Interpolated quantities are obtained through a Clough-Tocher interpolator to our whole data set.

	N_A $[\mathrm{cm}^{-3}]$	κ $\left[\frac{\mathrm{W}}{\mathrm{m\cdot K}}\right]$	σ $\left[\frac{\mathrm{S}}{\mathrm{cm}}\right]$	S $\left[\frac{\mu\mathrm{V}}{\mathrm{K}}\right]$	$ZT\times10^2$
S_{exp} =331 $\mu\mathrm{V\,K}^{-1}$†	1.19×10^{19} - 1.24×10^{19}	34.1-40.5	187-199	329-332	1.8-1.6
S_{exp} =225.1 $\mu\mathrm{V\,K}^{-1}$†	4.00×10^{19} - 4.15×10^{19}	32.4-38.3	550-583	222-225	2.5-2.3

† These results correspond to the values for NWs of radius 30 (left) and 45 (right) nm.

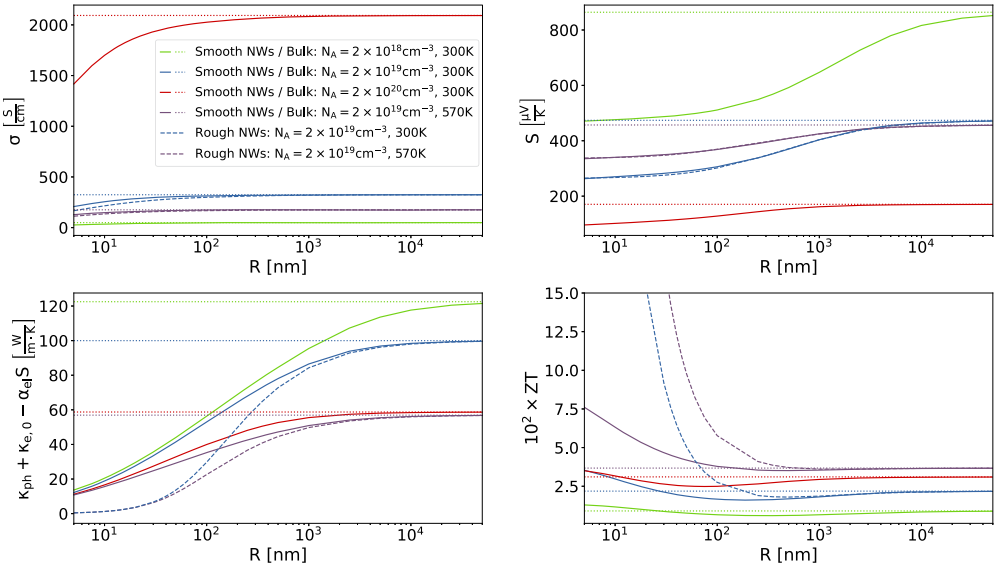

Fig. 8. Electrical conductivity, Seebeck coefficient, total thermal conductivity at zero electric current, and figure of merit as function of NW radius at 300 and 570 K and for several acceptor concentrations (B), without and with the inclusion of extreme surface roughness effects. Bulk values (dashed) are given as reference.

2.5. Effects of surface roughness

All the results we have presented so far correspond to smooth diffusive SiNWs, meaning that the surface roughness is not large enough to feature localized surface states, but large enough so that phonons hitting the surface boundary are diffusively scattered. As already mentioned, the SiNWs of Ref. [11] present extremely rough surfaces, which introduces additional phonon surface scattering and thus reduces κ.

We have added a model of extreme surface roughness in our calculations, according to the methodology described in Sec. 4.2. The results are shown in Fig. 8. We observe there that the effect of a large surface roughness is to decrease the phonon thermal conductivity, while keeping σ and S basically unaffected. Consequently, at 300 K the NW radius for which ZT becomes larger than the bulk value is increased to around 200 nm, thus reconciling our calculations with the qualitative experimental observations that ZT is above the bulk value for rough NWs [11]. At a higher temperature of 570 K there would barely be any reduction of ZT with respect to bulk in rough NWs. We also note that, at 570 K, the extent and amount of ZT reduction with respect to bulk is less than at 300 K.

3. Discussion

In this work, we have presented *ab initio* calculations of effective thermoelectric properties for Si nanowires of several radii and doping concentrations, using density functional theory data to iteratively

solve a suppressed coupled electron-phonon Boltzmann transport equation taking boundaries into account through the appropriate constraints on the non-homogeneous EPBTE. This is further simplified to a tractable problem by the use of cross-sectional averages (i.e. suppressed EPBTE). In fact, we have extended the `elphbolt` package by implementing such an approach, so that it can provide effective quantities for NWs. This allows unprecedented precision in the obtaining of dragged effective thermoelectric quantities.

Furthermore, we also provide a detailed explanation for the behavior of effective thermoelectric parameters and figure of merit as a function of the NW radius, showing the interplay of the different scales for phonons and electrons. Additionally, we show that there is a limited range of radii and doping concentration (B) in which the thermoelectric properties are enhanced by nanostructuring. In fact, outside that range the suppression of the drag contribution to S reduces thermoelectric efficiency below the bulk level, hence indicating that arbitrary nanostructuring does not necessarily ensure better thermoelectric efficiency. This leads to the observation that, in systems where there is a strong contribution of phonon drag to the Seebeck coefficient, nanostructuring may be detrimental to the thermoelectric performance of the material, by reducing S faster than the lattice thermal conductivity. We have also seen that the presence of extremely rough surfaces introduces a factor further reducing the thermal conductivity, while leaving other magnitudes practically unaffected, which mitigates the reduction of ZT for large NW diameters.

Finally, we provide a data set and a fitting equation for the computation of the Seebeck coefficient in NWs as a function of both acceptor concentration and radius. We show that such a fit can be used for the electrical determination of the doping concentration in Si NWs based on S, offering an improved accuracy when compared to standard methods.

4. Methods

4.1. Including boundary effects in the EPBTE beyond Matthiessen's rule

The customary approach to include boundary effects coming from the nanostructuring is through the introduction of a Casimir boundary scattering term [63],

$$[\tau_I^{\text{Boundary}}]^{-1} = \frac{(1-p)||\mathbf{v}_I||}{(1+p)L}, \tag{4}$$

where τ_I^{Boundary} is the boundary scattering of the I-th mode/state (from now on we make use of lower case Latin alphabet letters for electronic states, lower case Greek alphabet letters for phonon modes, and upper case Latin alphabet letters for cases in which the same equation applies to both systems), $p \in [0,1]$ is the specularity parameter, $\mathbf{v}_I$ is the group velocity of the I-th mode/state, and L is the limiting length of the system. This boundary scattering term is included via Matthiessen's rule [63,35,36]; hence we dub this approach as Casimir-Matthiessen's (CM). However, we note that this formalism does not consider the system's geometry, breaks energy conservation of the linearized scattering operator, and –what is more important– has been demonstrated to break down for some systems such as nanoribbons [49], thus making this solution potentially inadequate for an accurate description of thermoelectric properties in nanostructures. In principle, a more rigorous way to account for boundaries of the nanostructured systems, such as those of interest for thermoelectric applications, consists in going beyond the homogeneity approximation.

To this end, one needs to resort to the linearized non-homogeneous time-independent EPBTE [63,64]:

$$\begin{cases} \nabla T_{\text{ref}} \cdot \mathbf{v}_i \frac{\partial f_i^0}{\partial T_{\text{ref}}} + e\mathbf{E} \cdot \mathbf{v}_i \frac{\partial f_i^0}{\partial \epsilon_i} + \mathbf{v}_i \cdot \nabla f_i^d(\mathbf{r}) \\ \quad = \sum_\beta M_{i\beta} n_\beta^d(\mathbf{r}) + \sum_j D_{ij} f_j^d(\mathbf{r}) \\ \nabla T_{\text{ref}} \cdot \mathbf{v}_\lambda \frac{\partial n_\lambda^0}{\partial T_{\text{ref}}} + \mathbf{v}_\lambda \cdot \nabla n_\lambda^d(\mathbf{r}) = \sum_\beta (A_{\lambda\beta} + B_{\lambda\beta}) n_\beta^d(\mathbf{r}) + \sum_j C_{\lambda j} f_j^d(\mathbf{r}) \end{cases} \tag{5}$$

where the phonon (n) and electron (f) distributions have been expanded as an equilibrium contribution –n^0 and f^0, which are well described by Bose-Einstein and Fermi-Dirac distributions at a given reference temperature, T_{ref}, and electrochemical potential, μ_{ref}– and small deviation from these (n^d and f^d) so that the linearization of the scattering operator holds; ε_i is the energy of the i-th electronic state, e is the electron charge, $\mathbf{E}$ is a homogeneous electric field, and M, D, A, B, and C are the linearized scattering operator terms [see Eqs. (A.1)-(A.5) below], being M and C the terms responsible for the coupling between electronic and phononic systems (i.e. drag).

Not only that, but one needs also to define an appropriate set of boundary conditions for phonons and electrons arriving at a boundary at $\mathbf{r}_B$:

$$f_j^d(\mathbf{r}_B) = \frac{1}{N_{\text{k}}} \sum_{\{i\,:\,\mathbf{v}_i \cdot \hat{\mathbf{e}}_\perp^{in} > 0\}} P_{i\to j}^{\text{Boundary}} f_i^d(\mathbf{r}_B) \;:\; \mathbf{v}_j \cdot \hat{\mathbf{e}}_\perp^{in} < 0, \tag{6}$$

$$n_\beta^d(\mathbf{r}_B) = \frac{1}{N_{\text{q}}} \sum_{\{\lambda\,:\,\mathbf{v}_\lambda \cdot \hat{\mathbf{e}}_\perp^{in} > 0\}} P_{\lambda\to\beta}^{\text{Boundary}} n_\lambda^d(\mathbf{r}_B) \;:\; \mathbf{v}_\beta \cdot \hat{\mathbf{e}}_\perp^{in} < 0. \tag{7}$$

Here, N_{k} (N_{q}) is the number of points in the electronic k-mesh (phononic q-mesh), $P_{j\to i}^{\text{Boundary}}$ ($P_{\lambda\to\beta}^{\text{Boundary}}$) is the probability of an electron (phonon) in the i-th state (λ-th mode) to be scattered to j state (β mode) and $\hat{\mathbf{e}}_\perp^{in}$ is the normal vector to boundary pointing into the material. This last equation can be further simplified by noting that from all phonons and electrons arriving at the boundary, only a fraction p is specularly reflected whilst the rest are diffusively scattered, so that in the steady-state they will only contribute to the equilibrium distribution [63]. In other words, a perfect diffuse boundary absorbs all phonons and electrons arriving at it, which are then reemitted from such a boundary at a rate and distribution depending on the boundary temperature [65]. This allows simplifying boundary scattering to

$$f_j^d(\mathbf{r}_B) = p f_i^d(\mathbf{r}_B) \;:\; \mathbf{v}_j \cdot \hat{\mathbf{e}}_\perp^{in} < 0 \text{ and } \mathbf{v}_j = \mathbf{v}_i - 2(\mathbf{v}_i \cdot \hat{\mathbf{e}}_\perp^{in})\hat{\mathbf{e}}_\perp^{in}, \tag{8}$$

$$n_\beta^d(\mathbf{r}_B) = p n_\lambda^d(\mathbf{r}_B) \;:\; \mathbf{v}_\beta \cdot \hat{\mathbf{e}}_\perp^{in} < 0 \text{ and } \mathbf{v}_\beta = \mathbf{v}_\lambda - 2(\mathbf{v}_\lambda \cdot \hat{\mathbf{e}}_\perp^{in})\hat{\mathbf{e}}_\perp^{in}. \tag{9}$$

Although in principle, one can iteratively solve Eq. (5) under the constraints of Eqs. (8) and (9), its solution would require a discretization in space. Even for the simplest case of fully diffusive boundaries ($p = 0$), this is from a computational point of view impractical, owing to the enormous required memory resources and computational time for its solution. Indeed, for the case in which there is no other spatial dependence other than that coming from the mode/state itself, as it would be the case for an RTA collision operator, there exists an analytic solution developed by Chambers [47,63]. Therefore, a starting point to simplify Eq. (5) to a more bearable form is to approximate the coupling with other modes/states—that is the RTA deviations—by their cross-sectional average along the direction of interest (i.e. the unbounded direction) [24,66]; thus arriving to:

$$\begin{cases} f_i^d(\mathbf{r}) = \tau_i \left[-\nabla T_{\text{ref}} \cdot \mathbf{v}_i \frac{\partial f_i^0}{\partial T_{\text{ref}}} - e\mathbf{E} \cdot \mathbf{v}_i \frac{\partial f_i^0}{\partial \epsilon_i} + \sum_{j\neq i} D_{ij} \bar{f}_j^d + \sum_\beta M_{i\beta} \bar{n}_\beta^d \right] \\ \qquad \times \left(1 + K_i(\mathbf{r}, \mathbf{r}_B) e^{-\frac{|\mathbf{r}-\mathbf{r}'_B|}{\tau_i |\mathbf{v}_i|}} \right) \\ n_\lambda^d(\mathbf{r}) = \tau_\lambda \left[-\nabla T_{\text{ref}} \cdot \mathbf{v}_\lambda \frac{\partial n_\lambda^0}{\partial T_{\text{ref}}} + \sum_{\beta\neq\lambda} (A_{\lambda\beta} + B_{\lambda\beta}) \bar{n}_\beta^d + \sum_j C_{\lambda j} \bar{f}_j^d \right] \\ \qquad \times \left(1 + K_\lambda(\mathbf{r}, \mathbf{r}'_B) e^{-\frac{|\mathbf{r}-\mathbf{r}'_B|}{\tau_\lambda |\mathbf{v}_\lambda|}} \right) \end{cases}, \tag{10}$$

where $\mathbf{r}'_B$ is the boundary position the particle will ballistically intercept by moving backwards in time, so that $\mathbf{v}_I \parallel |\mathbf{r} - \mathbf{r}'_B|$; $K_I(\mathbf{r}, \mathbf{r}'_B)$ is an intricate function determined by boundary conditions; $\bar{f}_i^d$ and $\bar{n}_\lambda^d$ are the

cross-sectional averages of the deviational distribution; and $\tau_i = -\frac{1}{D_{ii}}$ and $\tau_\lambda = -\frac{1}{A_{\lambda\lambda}+B_{\lambda\lambda}}$ are the electronic and phononic RTA lifetimes. For fully diffusive boundaries, $K_I(\mathbf{r},\mathbf{r}'_B)$ reduces to -1, and thus the cross-sectional deviational distributions necessary to compute the effective thermoelectric properties can be computed as

$$\begin{cases} \bar{f}_i^d = \tau_i^{\text{nano}} \left[-\nabla T_{\text{ref}} \cdot \mathbf{v}_i \frac{\partial f_i^0}{\partial T_{\text{ref}}} - e\mathbf{E} \cdot \mathbf{v}_i \frac{\partial f_i^0}{\partial \epsilon_i} + \sum_{j\neq i} D_{ij} \bar{f}_j^d + \sum_\beta M_{i\beta} \bar{n}_\beta^d \right] \\ \bar{n}_\lambda^d = \tau_\lambda^{\text{nano}} \left[-\nabla T_{\text{ref}} \cdot \mathbf{v}_\lambda \frac{\partial n_\lambda^0}{\partial T_{\text{ref}}} + \sum_{\beta\neq\lambda} (A_{\lambda\beta} + B_{\lambda\beta}) \bar{n}_\beta^d + \sum_j C_{\lambda j} \bar{f}_j^d \right] \end{cases}, \tag{11}$$

with

$$\tau_I^{\text{nano}} = \tau_I S_I^{\text{nano}} = \tau_I \int_{A_c} \left(1 - e^{-\frac{|\mathbf{r}-\mathbf{r}'_B|}{\tau_I |\mathbf{v}_I|}} \right) dA; \tag{12}$$

here A_c refers to the cross-section, and S_I^{nano} is a suppression factor $\in [0,1]$ which accounts for the effect of the surface over the deviational distribution with respect to the bulk one.

Therefore, the effective solution of the EPBTE for highly symmetric systems, henceforth referred as *suppressed*, is rather similar to the bulk solution, with the exception that lifetimes are suppressed by geometrical factors, which break the crystalline symmetry. Indeed, it is straightforward to demonstrate that this last statement holds for the usual expansion of deviations in terms of the leading fields (i.e. thermal gradient and electric field) [34,67,35], and thus the solution can be obtained by replacing the lifetimes by their suppressed counterparts [66]. In particular, for the case of cylindrical NWs, the suppression factors (S_I^{NW}) can be analytically calculated, by evaluating the integral in modified cylindrical coordinates with the z-axis pointing to the periodic direction defined by the unitary vector $\hat{\mathbf{u}}$, yielding:

$$S_I^{\text{NW}} = 1 - \frac{2M_I^{\text{NW}}}{\pi R} - \frac{M_I^{\text{NW}}}{R} \left[\mathcal{I}_1 \left(\frac{2R}{M_I^{\text{NW}}} \right) - \mathcal{L}_{-1} \left(\frac{2R}{M_I^{\text{NW}}} \right) \right] = 1 - \frac{2M_I^{\text{NW}}}{\pi R} + \frac{2M_I^{\text{NW}}}{\pi R^2} \int_0^R \exp\left(-2\frac{\sqrt{R^2-x^2}}{M_I^{\text{NW}}} \right) dx \tag{13}$$

$$M_I^{\text{NW}} = \|\mathbf{v}_I - (\mathbf{v}_I \cdot \hat{\mathbf{u}})\hat{\mathbf{u}}\| \tau_I, \tag{14}$$

where R is the NW radius, and $\mathcal{I}_1$ and $\mathcal{L}_{-1}$ are the modified Bessel and Struve functions of order 1 and -1, respectively. The integral form included in Eq. (13) is written for computational reasons; as the enormous floating point error coming from a direct subtraction between modified Bessel and Struve functions makes its direct solution computationally unfeasible, so that one needs to rely on the numerical solution of the integral form by the trapezoidal rule to obtain reliable results of the suppression factor.

Although some of the approximations –such as the replacement of the RTA deviations by their cross-sectional average– can seem rather crude, it is worth noting that this approach has not only proven to provide results in excellent agreement with more accurate Monte Carlo based solutions of the phonon BTE [68], but to accurately reproduce experimental results [11,12] for thermal transport (see the discussion below). At the same time, however, we stress that while this approach is in principle much more accurate than CM, it still relies on the use of bulk properties and of 3D periodic formulas (e.g. 3D non-analytic correction for phonons in polar materials); so that the effect of surface effects is disregarded. Moreover, our approach ignores any quantization or confinement effect over electrons and/or phonons for extremely thin NWs—which is expected to be important for diameters smaller than 10 nm [46,45]—, which combined with the lack of surface states and donor/acceptor deactivation due to dielectric mismatch [57], makes our approach unsuited for very thin and/or low-doped-uncoated NWs where such effects might be important. As mentioned above, nonetheless, this is not an important limitation for the NWs used in practical devices, as they usually have significantly larger diameters.

To summarize, the CM solves the linearized homogeneous PBTE, does not take into account the system's geometry (i.e. it directly scatters phonons traveling parallel to periodic direction, something unphysical), it is introduced at the RTA-level (it does not conserve energy), and it has been proven to breakdown for some nanosystems (e.g. nanoribbons). In contrast, the suppressed approach derives directly from averaging the non-homogeneous PBTE in the full-linearized approach (i.e. beyond the RTA) and, consequently, does not suffer from such flaws. The latter is, as the former, still excluding several effects that might be important, especially for thin and/or extremely rough nanowires, namely it does not consider surface states (bulk properties are used), possible donor/acceptor deactivation due to dielectric mismatch, and/or quantization effects.

4.2. Roughness treatment

As mentioned in the previous section, none of the detailed approaches account for surface states. Therefore, for the modeling of extremely rough NWs, such as those of Refs. [11] and [12], an additional scattering channel for phonons accounting for such surface states should be considered. Unfortunately, the addition of these terms within the suppressed approach, albeit theoretically possible, would require to solve Eq. (12) not only in the plane normal to the transport direction, but along a relative large representative section over it—i.e. a surface profile sample with the equivalent root mean square average (δ) and correlation length (η)—, further complicating the solution. Alternatively, in the homogeneous approach, that is CM, it is possible to introduce the effect of surface state scattering through an additional scattering rate based on an semi-empirical approximation derived from a bond-order model as [69,55]:

$$\tau_{\text{Roughness},\lambda}^{-1} = A \cdot SVR \cdot \omega_\lambda^4, \tag{15}$$

where A is 1.86×10^{-51} s^{-1} for Si [55], and SVR is the surface-to-volume ratio, which is defined as:

$$SVR = \frac{2\int_0^L y(x)\sqrt{1+y'(x)^2}dx}{LR^2}. \tag{16}$$

Here, L is the length of the NW (i.e. the length of the computational profile used to represent the infinite NW), and $y(x)$ is the surface profile, which can be computed from the Gaussian correlation function ($C(x) = \delta^2 e^{-x^2/\eta^2}$) following [70,69]:

$$y(x) = \mathcal{F}_x^{-1}[\sqrt{\mathcal{F}_x[C(x)](q)}e^{\phi_q}](x) + R, \tag{17}$$

where $\mathcal{F}_x[f(x)](q)[\mathcal{F}_x^{-1}[f(q)](x)]$ is the [inverse] Fourier transform of the given function f, and is e^{ϕ_q} a random odd phase (i.e. $e^{\phi_{-q}} = -e^{\phi_q}$, with ϕ uniformly sampled between $[-\pi,\pi]$). We find it worth to mention that this model is derived from perturbation theory, and will thus break extremely rough surfaces for thin NWs.

4.3. Density-functional calculations and solution of the coupled EPBTE

The calculation of all the quantities needed to solve the EPBTE was done within the framework of Density Functional Theory (DFT). The unit cell used as a basis for the whole set of calculations was optimized until strict limits for stress (3×10^{-3} GPa) and forces (5×10^{-4} eV Å^{-1}) were attained. These optimizations were conducted using the plane-wave `Quantum Espresso` [71,72] code with a norm-conserving pseudopotential [73], using a cutoff of 45 Ry, and a $12 \times 12 \times 12$ Γ-centered k-mesh. Local Density Approximation (LDA) for the exchange-correlation as parametrized by Perdew and Zunger [74] to Ceperley-Alder [75] data was used. Harmonic interatomic force constants (IFCs)

and the first-derivative of the potential with respect to phonon perturbations were obtained using Density Perturbation Functional Theory (DPFT), as implemented in `PHonon` package included within `Quantum Espresso` suit [71,72], using a $6\times6\times6$ Γ-centered k-mesh and a strict convergence limit of 1.0×10^{-13} Ry. Anharmonic IFCs were computed using the supercell method as implemented thirdorder.py [66], using `Quantum Espresso` as force calculator, with a $5\times5\times5$ supercell and a cutoff for the interactions up to the 6^{th} nearest neighbor. The computation of electron-phonon matrix elements and Hamiltonian in the real space was done using `EPW` package [76], through the wannierisation up to the 8^{th} band, using 8 sp^3 Si-centered orbitals for the initial projection, and a disentanglement window up to 17.5 eV with states below 9.5 eV frozen. Electronic-charged impurity matrix elements were obtained using the first Born approximation, by considering the impurity potential to be described by a static screened Coulomb potential, namely a Yukawa potential, as implemented in the `elphbolt` code (see Eqs. (9)-(11) of Ref. [35]). Electron-electron interaction has not been considered on our calculations, something that for high-concentrations (i.e. $\gtrsim 1\times10^{20}\,\mathrm{cm}^{-3}$) renders an overestimated bulk electrical conductivity to 2 to 4 times the experimental results [35]).

To compute the effective thermoelectric properties, we have used a modified version of `elphbolt` version, in which we have implemented the computation of effective thermoelectric properties for NWs, by iteratively solving the suppressed EPBTE. Consequently, effective thermoelectric properties—electrical conductivity (σ), the Seebeck coefficient (S), the electronic thermal response to an electric field (α_{el}), the electronic thermal conductivity without applied electric field ($\kappa_{\mathrm{el},0}$), the phonon thermal response to an electric field (α_{ph}), the phonon thermal conductivity (κ_{ph}), and the total thermal conductivity at zero-current (κ)—are obtained as:

$$\sigma^{\mathrm{eff}} = \frac{2e}{N_{\mathrm{k}}V_{\mathrm{uc}}k_B T_{\mathrm{ref}}}\sum_i f_i^0(1-f_i^0)v_i^n\bar{J}_i, \tag{18}$$

$$(\sigma S)^{\mathrm{eff}} = -\frac{2e}{N_{\mathrm{k}}V_{\mathrm{uc}}k_B T_{\mathrm{ref}}}\sum_i f_i^0(1-f_i^0)v_i^n\bar{H}_i, \tag{19}$$

$$\alpha_{\mathrm{el}}^{\mathrm{eff}} = -\frac{2}{N_{\mathrm{k}}V_{\mathrm{uc}}k_B T_{\mathrm{ref}}}\sum_i(\varepsilon_i-\mu_{\mathrm{ref}})f_i^0(1-f_i^0)v_i^n\bar{J}_i, \tag{20}$$

$$\kappa_{\mathrm{el},0}^{\mathrm{eff}} = \frac{2}{N_{\mathrm{k}}V_{\mathrm{uc}}k_B T_{\mathrm{ref}}}\sum_i(\varepsilon_i-\mu_{\mathrm{ref}})f_i^0(1-f_i^0)v_i^n\bar{H}_i, \tag{21}$$

$$\alpha_{\mathrm{ph}}^{\mathrm{eff}} = -\frac{1}{N_{\mathrm{q}}V_{\mathrm{uc}}k_B T_{\mathrm{ref}}}\sum_\lambda \hbar\omega_\lambda n_\lambda^0(n_\lambda^0+1)v_\lambda^n\bar{G}_\lambda, \tag{22}$$

$$\kappa_{\mathrm{ph}}^{\mathrm{eff}} = \frac{1}{N_{\mathrm{q}}V_{\mathrm{uc}}k_B T_{\mathrm{ref}}}\sum_\lambda \hbar\omega_\lambda n_\lambda^0(n_\lambda^0+1)v_\lambda^n\bar{F}_\lambda, \tag{23}$$

$$\kappa^{\mathrm{eff}} = \kappa_{\mathrm{ph}}^{\mathrm{eff}} + \kappa_{\mathrm{el},0}^{\mathrm{eff}} - \alpha_{\mathrm{el}}^{\mathrm{eff}}S^{\mathrm{eff}} \tag{24}$$

where V_{uc} is the volume of the unit cell, k_B is the Boltzmann constant, $v_I^n = \mathbf{v}_I\cdot\hat{\mathbf{u}}$, $\hbar$ is the reduced Planck constant, ω_λ is the phonon frequency, and $\bar{H}_i(\bar{F}_\lambda)$ and $\bar{J}_i(\bar{G}_\lambda)$ are the cross-sectional average of the suppressed electron (phonon) deviation functions due to applied thermal gradient and electric fields, respectively. These deviation functions are related to cross-sectional averages defined in Eq. (11) as:

$$\bar{f}_i^d = -\frac{f_i^0(1-f_i^0)}{k_B T_{\mathrm{ref}}}(\nabla T_{\mathrm{ref}}^n\bar{H}_i + E^n\bar{J}_i), \tag{25}$$

$$\bar{n}_\lambda^d = -\frac{n_\lambda^0(n_\lambda^0+1)}{k_B T_{\mathrm{ref}}}(\nabla T_{\mathrm{ref}}^n\bar{F}_\lambda + E^n\bar{G}_\lambda), \tag{26}$$

where $\nabla T_{\mathrm{ref}}^n$ and E^n are the thermal gradient and electric field applied along the transport (unbounded) direction, respectively.

Regarding the details on the EPBTE resolution, this last was solved using a Γ-centered $50\times50\times50$ ($150\times150\times150$) q-mesh (k-mesh) for phonons (electrons), with an active window for electronic states of ±0.45 eV around the computed chemical potential for the given temperature and doping concentration (see below for the chemical potential as function of the doping). The beyond and dragged solutions were iteratively converged until the relative change in all the transport coefficients was less than 1.0×10^{-4}. Furthermore, owing to the inability of DFT to provide a reliable band gap we have modified the code, implementing a scissor operator for conduction bands. We have set the value of such a scissor operator to the value that makes the gap (E_g) to match its experimental value at a given temperature (T), as given by Varshni's formula for Si [77]:

$$E_g(T) = 1.1557 - \frac{7.021T^2}{T+1108}, \tag{27}$$

where energy is given in eV and temperature in K. This last, provides at 300 K a gap value of approximately 1.110 eV, so that a scissor operator of ≈0.615 eV is applied for the DFT gap of ≈0.496 eV to match such a value.

Finally, we note that through all the manuscript, we have supposed fully ionized charged impurities, together with the assumption that the intrinsic concentration is much smaller than the one coming from these impurities. The former is justified as we are assuming shallow impurities—B and P—, which are almost fully ionized at the temperature of our simulations, namely room temperature; while the latter is true as the intrinsic carrier concentration of silicon at room temperature is $9.65\times10^9\,\mathrm{cm}^{-3}$ [78]. Therefore, the carrier concentration can be approximated by the doping one in our case, which is relatively high B (acceptor) and P (donor) dopant concentrations at room temperature.

CRediT authorship contribution statement

Martí Raya-Moreno: Writing – review & editing, Writing – original draft, Software, Investigation, Data curation, Conceptualization. **Riccardo Rurali:** Writing – review & editing, Validation, Supervision, Resources, Funding acquisition. **Xavier Cartoixà:** Writing – review & editing, Validation, Supervision, Resources, Funding acquisition, Conceptualization.

Declaration of competing interest

The authors declare that they have no known competing financial interests or personal relationships that could have appeared to influence the work reported in this paper.

Data availability

The data that support the findings of this study are available from the authors upon reasonable request.

Acknowledgements

M.R-M and R.R acknowledge financial support from MCIN/AEI/10.13039/501100011033 under grant PID2020-119777GB-I00, and the Severo Ochoa Centres of Excellence Program under grant CEX2019-000917-S, and by the Generalitat de Catalunya under grant 2021 SGR 01519. X.C acknowledges financial support by Spain's Ministerio de Ciencia, Innovación y Universidades under Grant No. RTI2018-097876-B-C21 (MCIU/AEI/FEDER, UE), and Ministerio de Ciencia e Innovación under Grant No. PID2021-127840NB-I00 (MICINN/AEI/FEDER, UE). The authors thankfully acknowledge the computer resources, technical expertise and assistance provided by the Centro de Supercomputación de Galicia (CESGA).

Appendix A. Linearized scattering operator terms

The linearized collision operator terms for a spin-degenerate electrophononic system are:

$$A_{\lambda\beta} = \sum_{\alpha\gamma\xi} P^{3\text{ph}}_{\alpha+\gamma\to\xi}\Big[(n^0_\xi - n^0_\alpha)\delta_{\lambda\alpha}\delta_{\beta\gamma} + (n^0_\alpha + n^0_\gamma + 1)\delta_{\lambda\alpha}\delta_{\beta\xi} + (n^0_\xi - n^0_\gamma)\delta_{\lambda\alpha}\delta_{\beta\lambda}\Big] + \frac{1}{2}\sum_{\alpha\gamma\xi} P^{3\text{ph}}_{\alpha\to\gamma+\xi}\Big[(n^0_\xi - n^0_\alpha)\delta_{\lambda\alpha}\delta_{\beta\gamma} + (n^0_\gamma - n^0_\alpha)\delta_{\lambda\alpha}\delta_{\beta\xi} - (n^0_\xi + n^0_\gamma + 1)\delta_{\lambda\alpha}\delta_{\beta\lambda}\Big] + \sum_{\alpha\gamma}(P^{\text{iso}}_{\alpha\to\gamma} + P^{\text{subs}}_{\alpha\to\gamma})\left[\delta_{\lambda\alpha}\delta_{\beta\gamma} - \delta_{\lambda\alpha}\delta_{\beta\lambda}\right]. \tag{A.1}$$

$$B_{\lambda\beta} = 2\sum_{i\alpha j} P^{\text{e-ph}}_{i+\alpha\to j}(f^0_j - f^0_i)\delta_{\lambda\alpha}\delta_{\beta\lambda}, \tag{A.2}$$

$$C_{\lambda j} = 2\sum_{i\alpha k} P^{\text{e-ph}}_{i+\alpha\to k}[(-f^0_k - n^0_\alpha)\delta_{\lambda\alpha}\delta_{ji} + (-f^0_i + n^0_\alpha + 1)\delta_{\lambda\alpha}\delta_{jk}], \tag{A.3}$$

$$D_{ij} = \sum_{k\alpha l} P^{\text{e-ph}}_{k\to l+\alpha}[(f^0_l - n^0_\alpha - 1)\delta_{ki}\delta_{ji} + (f^0_k + n^0_\alpha)\delta_{ki}\delta_{jl}] + \sum_{k\alpha l} P^{\text{e-ph}}_{k+\alpha\to l}[-(f^0_l + n^0_\alpha)\delta_{ki}\delta_{ji} + (-f^0_k + n^0_\alpha + 1)\delta_{ki}\delta_{jl}] + \sum_{sm} P^{\text{e-chimp}}_{s\to m}\left[\delta_{is}\delta_{jm} - \delta_{is}\delta_{ji}\right], \tag{A.4}$$

and

$$M_{i\beta} = \sum_{k\alpha l} P^{\text{e-ph}}_{k\to l+\alpha}(f^0_l - f^0_k)\delta_{ik}\delta_{\beta\alpha} + \sum_{k\alpha l} P^{\text{e-ph}}_{k+\alpha\to l}(f^0_l - f^0_k)\delta_{ik}\delta_{\beta\alpha}, \tag{A.5}$$

where $P^{3\text{ph}}_{\alpha+\gamma\to\xi}$ ($P^{3\text{ph}}_{\alpha\to\gamma+\xi}$) is the three-phonon intrinsic (i.e. scattering rate without occupation weights) transition rate due to three-phonon absorption (emission) processes (see Eqs. (7) and (8) of Ref. [66] for the definition of such terms), $P^{\text{iso}}_{\alpha\to\gamma}$ and $P^{\text{subs}}_{\alpha\to\gamma}$ are the intrinsic transition rate due to isotopic and mass substitutional scattering, respectively, computed using Tamura's model [79] (see Eq. (10) of Ref. [66] for the definition of such a term), $P^{\text{e-ph}}_{i+\alpha\to k}$ ($P^{\text{e-ph}}_{i\to\alpha+k}$) is the intrinsic transition rate due to electron-phonon interaction (see Eqs. (8) and (12) of Ref. [35] for the definition of such terms), and $P^{\text{e-chimp}}_{i\to j}$ is the intrinsic transition rate due to charged impurity scattering (see Eq. (11) of Ref. [35] for the definition of such a term). We note that on the original implementation of `elphbolt`, as well on our modified version, out-of-diagonal terms for isotopic, mass substitutional, and charged impurity scattering are deprecated; nonetheless the introduction of such terms introduces an error no higher than a 3% for phonon and electron thermal response to an electric field, while providing much lower errors for the rest of quantities.

Appendix B. Chemical potential as function of the doping

Here (see Fig. 9) we provide the chemical potential as function of donor/acceptor concentration for bulk Si at 300 K with an applied scissor operator such that band-gap is set at ∼1.11 eV, for the case of fully ionized B and P impurities, and assuming that the intrinsic contribution is negligible.

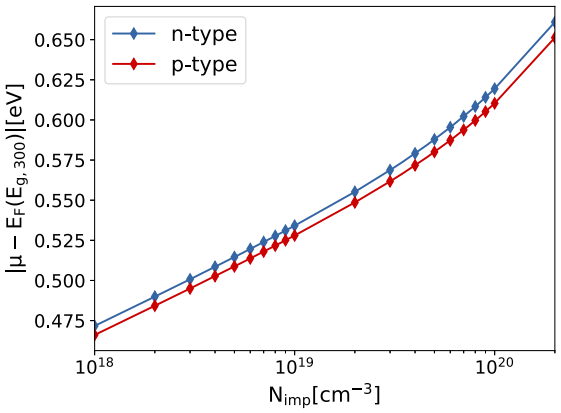

Fig. 9. Absolute value of the chemical potential relative to Fermi level as function of *n*-type(red) and *p*-type (blue) doping concentration for bulk Si at 300 K with a scissor-corrected band gap of ≈1.110 eV. The values are computed for the case of fully ionized P (donor) and B (acceptor) impurities, and assuming that the intrinsic contribution is negligible. Note that $\mu - E_F(E_{g,300}) < 0$ for *p*-type NWs.

References

[1] A.J. Minnich, M.S. Dresselhaus, Z.F. Ren, G. Chen, Bulk nanostructured thermoelectric materials: current research and future prospects, Energy Environ. Sci. 2 (2009) 466–479, https://doi.org/10.1039/B822664B.

[2] M. Zebarjadi, K. Esfarjani, M.S. Dresselhaus, Z.F. Ren, G. Chen, Perspectives on thermoelectrics: from fundamentals to device applications, Energy Environ. Sci. 5 (2012) 5147–5162.

[3] G. Benenti, G. Casati, K. Saito, R.S. Whitney, Fundamental aspects of steady-state conversion of heat to work at the nanoscale, Phys. Rep. 694 (2017) 1–124.

[4] D. Beretta, N. Neophytou, J.M. Hodges, M.G. Kanatzidis, D. Narducci, M. Martín-Gonzalez, M. Beekman, B. Balke, G. Cerretti, W. Tremel, A. Zevalkink, A.I. Hofmann, C. Müller, B. Dörling, M. Campoy-Quiles, M. Caironi, Thermoelectrics: from history, a window to the future, Mater. Sci. Eng., R Rep. 138 (2019) 100501.

[5] C. Artini, G. Pennelli, P. Graziosi, Z. Li, N. Neophytou, C. Melis, L. Colombo, E. Isotta, K. Lohani, P. Scardi, A. Castellero, M. Baricco, M. Palumbo, S. Casassa, L. Maschio, M. Pani, G. Latronico, P. Mele, F.D. Benedetto, G. Contento, M.F.D. Riccardis, R. Fucci, B. Palazzo, A. Rizzo, V. Demontis, D. Prete, M. Isram, F. Rossella, A. Ferrario, A. Miozzo, S. Boldrini, E. Dimaggio, M. Franzini, S. Galliano, C. Barolo, S. Mardi, A. Reale, B. Lorenzi, D. Narducci, V. Trifiletti, S. Milita, A. Bellucci, D.M. Trucchi, Roadmap on thermoelectricity, Nanotechnology 34 (29) (2023) 292001.

[6] A. Shakouri, Recent developments in semiconductor thermoelectric physics and materials, Annu. Rev. Mater. Res. 41 (1) (2011) 399–431, https://doi.org/10.1146/annurev-matsci-062910-100445.

[7] M.G. Kanatzidis, Nanostructured thermoelectrics: the new paradigm?, Chem. Mater. 22 (3) (2010) 648–659, https://doi.org/10.1021/cm902195j.

[8] C. Wood, High-temperature thermoelectric energy conversion—II. Materials survey, Energy Convers. Manag. 24 (4) (1984) 331–343, https://doi.org/10.1016/0196-8904(84)90013-X, https://www.sciencedirect.com/science/article/pii/019689048490013X.

[9] G.A. Slack, New Materials and Performance Limits for Thermoelectric Cooling, CRC Press, Boca Raton, 1995.

[10] M. Maldovan, Sound and heat revolutions in phononics, Nature 503 (7475) (2013) 209–217.

[11] G. Gadea Díez, J.M. Sojo Gordillo, M. Pacios Pujadó, M. Salleras, L. Fonseca, A. Morata, A. Tarancón Rubio, Enhanced thermoelectric figure of merit of individual Si nanowires with ultralow contact resistances, Nano Energy 67 (2020) 104191, https://doi.org/10.1016/j.nanoen.2019.104191, https://www.sciencedirect.com/science/article/pii/S2211285519308985.

[12] J.M. Sojo-Gordillo, D. Estrada-Wiese, C. Duque-Sierra, G. Gadea-Díez, M. Salleras, L. Fonseca, A. Morata, A. Tarancón, Tuning the thermoelectric properties of boron-doped silicon nanowires integrated into a micro-harvester, Adv. Mater. Technol. 7 (10) (2022) 2101715, https://doi.org/10.1002/admt.202101715, https://onlinelibrary.wiley.com/doi/abs/10.1002/admt.202101715.

[13] A.I. Hochbaum, P. Yang, Semiconductor nanowires for energy conversion, Chem. Rev. 110 (1) (2010) 527–546.

[14] Z. Li, Q. Sun, X.D. Yao, Z.H. Zhu, G.Q.M. Lu, Semiconductor nanowires for thermoelectrics, J. Mater. Chem. 22 (2012) 22821–22831.

[15] M.Y. Swinkels, I. Zardo, Nanowire for heat conversion, J. Phys. D, Appl. Phys. 51 (35) (2018) 353001.

[16] R. Chen, J. Lee, W. Lee, D. Li, Thermoelectrics of nanowires, Chem. Rev. 119 (15) (2019) 9260–9302.

[17] F. Domínguez-Adame, M. Martín-González, D. Sánchez, A. Cantarero, Nanowires: a route to efficient thermoelectric devices, Physica E 113 (2019) 213–225.

[18] O. Caballero-Calero, M. Martín-González, Thermoelectric nanowires: a brief prospective, Scr. Mater. 111 (2016) 54–57.

[19] A.I. Boukai, Y. Bunimovich, J. Tahir-Kheli, J.-K. Yu, W.A. Goddard III, J.R. Heath, Silicon nanowires as efficient thermoelectric materials, Nature 451 (7175) (2008) 168–171, https://doi.org/10.1038/nature06458.

[20] A.I. Hochbaum, R. Chen, R.D. Delgado, W. Liang, E.C. Garnett, M. Najarian, A. Majumdar, P. Yang, Enhanced thermoelectric performance of rough silicon nanowires, Nature 451 (7175) (2008) 163–167.

[21] C. Kittel, Solid State Physics, John Wiley & Sons, 1955.

[22] G.K. Madsen, J. Carrete, M.J. Verstraete, Boltztrap2, a program for interpolating band structures and calculating semi-classical transport coefficients, Comput. Phys. Commun. 231 (2018) 140–145, https://doi.org/10.1016/j.cpc.2018.05.010, https://www.sciencedirect.com/science/article/pii/S0010465518301632.

[23] M. Omini, A. Sparavigna, Beyond the isotropic-model approximation in the theory of thermal conductivity, Phys. Rev. B 53 (1996) 9064–9073, https://doi.org/10.1103/PhysRevB.53.9064, https://link.aps.org/doi/10.1103/PhysRevB.53.9064.

[24] W. Li, N. Mingo, L. Lindsay, D.A. Broido, D.A. Stewart, N.A. Katcho, Thermal conductivity of diamond nanowires from first principles, Phys. Rev. B 85 (2012) 195436, https://doi.org/10.1103/PhysRevB.85.195436, https://link.aps.org/doi/10.1103/PhysRevB.85.195436.

[25] A. Cepellotti, J. Coulter, A. Johansson, N.S. Fedorova, B. Kozinsky, Phoebe: a high-performance framework for solving phonon and electron Boltzmann transport equations, J. Phys. Mater. 5 (3) (2022) 035003, https://doi.org/10.1088/2515-7639/ac86f6.

[26] W. Li, Electrical transport limited by electron-phonon coupling from Boltzmann transport equation: an ab initio study of Si, al, and mos_2, Phys. Rev. B 92 (2015) 075405, https://doi.org/10.1103/PhysRevB.92.075405, https://link.aps.org/doi/10.1103/PhysRevB.92.075405.

[27] S. Poncé, E.R. Margine, F. Giustino, Towards predictive many-body calculations of phonon-limited carrier mobilities in semiconductors, Phys. Rev. B 97 (2018) 121201, https://doi.org/10.1103/PhysRevB.97.121201, https://link.aps.org/doi/10.1103/PhysRevB.97.121201.

[28] S. Poncé, W. Li, S. Reichardt, F. Giustino, First-principles calculations of charge carrier mobility and conductivity in bulk semiconductors and two-dimensional materials, Rep. Prog. Phys. 83 (3) (2020) 036501, https://doi.org/10.1088/1361-6633/ab6a43.

[29] J.-J. Zhou, J. Park, I.-T. Lu, I. Maliyov, X. Tong, M. Bernardi, Perturbo: a software package for ab initio electron–phonon interactions, charge transport and ultrafast dynamics, Comput. Phys. Commun. 264 (2021) 107970, https://doi.org/10.1016/j.cpc.2021.107970, https://www.sciencedirect.com/science/article/pii/S0010465521000837.

[30] H.J. Ryu, Z. Aksamija, D.M. Paskiewicz, S.A. Scott, M.G. Lagally, I. Knezevic, M.A. Eriksson, Quantitative determination of contributions to the thermoelectric power factor in Si nanostructures, Phys. Rev. Lett. 105 (2010) 256601, https://doi.org/10.1103/PhysRevLett.105.256601, https://link.aps.org/doi/10.1103/PhysRevLett.105.256601.

[31] J. Sadhu, H. Tian, J. Ma, B. Azeredo, J. Kim, K. Balasundaram, C. Zhang, X. Li, P.M. Ferreira, S. Sinha, Quenched phonon drag in silicon nanowires reveals significant effect in the bulk at room temperature, Nano Lett. 15 (5) (2015) 3159–3165, https://doi.org/10.1021/acs.nanolett.5b00267, pMID: 25831487.

[32] K. Fauziah, Y. Suzuki, T. Nogita, Y. Kamakura, T. Watanabe, F. Salleh, H. Ikeda, Effect of phonon-boundary scattering on phonon-drag factor in Seebeck coefficient of Si wire, AIP Adv. 10 (7) (07 2020) 075015, https://doi.org/10.1063/5.0016043.

[33] R. Sen, N. Vast, J. Sjakste, Role of dimensionality and size in controlling the drag Seebeck coefficient of doped silicon nanostructures: a fundamental understanding, Phys. Rev. B 108 (2023) L060301, https://doi.org/10.1103/PhysRevB.108.L060301.

[34] N.H. Protik, D.A. Broido, Coupled transport of phonons and carriers in semiconductors: a case study of *n*-doped GaAs, Phys. Rev. B 101 (2020) 075202, https://doi.org/10.1103/PhysRevB.101.075202, https://link.aps.org/doi/10.1103/PhysRevB.101.075202.

[35] N.H. Protik, C. Li, M. Pruneda, D. Broido, P. Ordejón, The elphbolt ab initio solver for the coupled electron-phonon Boltzmann transport equations, npj Comput. Mater. 8 (1) (2022) 28, https://doi.org/10.1038/s41524-022-00710-0.

[36] C. Li, N. Protik, P. Ordejón, D. Broido, Colossal phonon drag enhanced thermopower in lightly doped diamond, Mater. Today Phys. 27 (2022) 100740, https://doi.org/10.1016/j.mtphys.2022.100740, https://www.sciencedirect.com/science/article/pii/S2542529322001389.

[37] G.D. Mahan, L. Lindsay, D.A. Broido, The Seebeck coefficient and phonon drag in silicon, J. Appl. Phys. 116 (24) (2014) 245102, https://doi.org/10.1063/1.4904925, https://pubs.aip.org/aip/jap/article-pdf/doi/10.1063/1.4904925/15155485/245102_1_online.pdf.

[38] L.D. Hicks, M.S. Dresselhaus, Thermoelectric figure of merit of a one-dimensional conductor, Phys. Rev. B 47 (1993) 16631–16634, https://doi.org/10.1103/PhysRevB.47.16631.

[39] J. Zhou, B. Liao, B. Qiu, S. Huberman, K. Esfarjani, M.S. Dresselhaus, G. Chen, Ab initio optimization of phonon drag effect for lower-temperature thermoelectric energy conversion, Proc. Natl. Acad. Sci. 112 (48) (2015) 14777–14782, https://doi.org/10.1073/pnas.1512328112.

[40] J. Wei, L. Yang, Z. Ma, P. Song, M. Zhang, J. Ma, F. Yang, X. Wang, Review of current high-ZT thermoelectric materials, J. Mater. Sci. 55 (27) (2020) 12642–12704, https://doi.org/10.1007/s10853-020-04949-0.

[41] M.C. Wingert, S. Kwon, M. Hu, D. Poulikakos, J. Xiang, R. Chen, Sub-amorphous thermal conductivity in ultrathin crystalline silicon nanotubes, Nano Lett. 15 (4) (2015) 2605–2611, https://doi.org/10.1021/acs.nanolett.5b00167.

[42] L. Yang, Y. Yang, Q. Zhang, Y. Zhang, Y. Jiang, Z. Guan, M. Gerboth, J. Yang, Y. Chen, D.G. Walker, T.T. Xu, D. Li, Thermal conductivity of individual silicon nanoribbons, Nanoscale 8 (2016) 17895–17901, https://doi.org/10.1039/C6NR06302K.

[43] N. Neophytou, H. Kosina, Effects of confinement and orientation on the thermoelectric power factor of silicon nanowires, Phys. Rev. B 83 (2011) 245305, https://doi.org/10.1103/PhysRevB.83.245305.

[44] E.B. Ramayya, L.N. Maurer, A.H. Davoody, I. Knezevic, Thermoelectric properties of ultrathin silicon nanowires, Phys. Rev. B 86 (2012) 115328, https://doi.org/10.1103/PhysRevB.86.115328, https://link.aps.org/doi/10.1103/PhysRevB.86.115328.

[45] R. Rurali, Colloquium: structural, electronic, and transport properties of silicon nanowires, Rev. Mod. Phys. 82 (1) (2010) 427–449.

[46] Y.M. Niquet, A. Lherbier, N.H. Quang, M.V. Fernández-Serra, X. Blase, C. Delerue, Electronic structure of semiconductor nanowires, Phys. Rev. B 73 (2006) 165319, https://doi.org/10.1103/PhysRevB.73.165319, https://link.aps.org/doi/10.1103/PhysRevB.73.165319.

[47] R.G. Chambers, W.L. Bragg, The conductivity of thin wires in a magnetic field, Proc. R. Soc. Lond. Ser. A, Math. Phys. Sci. 202 (1070) (1950) 378–394, https://doi.org/10.1098/rspa.1950.0107, https://royalsocietypublishing.org/doi/abs/10.1098/rspa.1950.0107.

[48] W. Li, L. Lindsay, D.A. Broido, D.A. Stewart, N. Mingo, Thermal conductivity of bulk and nanowire $Mg_2Si_xSn_{1-x}$ alloys from first principles, Phys. Rev. B 86 (2012) 174307, https://doi.org/10.1103/PhysRevB.86.174307, https://link.aps.org/doi/10.1103/PhysRevB.86.174307.

[49] Z. Wang, N. Mingo, Absence of Casimir regime in two-dimensional nanoribbon phonon conduction, Appl. Phys. Lett. 99 (10) (2011) 101903, https://doi.org/10.1063/1.3635394.

[50] D. Zhao, X. Qian, X. Gu, S.A. Jajja, R. Yang, Measurement techniques for thermal conductivity and interfacial thermal conductance of bulk and thin film materials, J. Electron. Packag. 138 (4) (10 2016) 040802, https://doi.org/10.1115/1.4034605, https://asmedigitalcollection.asme.org/electronicpackaging/article-pdf/138/4/040802/6045875/ep_138_04_040802.pdf.

[51] Y. Ohishi, J. Xie, Y. Miyazaki, Y. Aikebaier, H. Muta, K. Kurosaki, S. Yamanaka, N. Uchida, T. Tada, Thermoelectric properties of heavily boron- and phosphorus-doped silicon, Jpn. J. Appl. Phys. 54 (7) (2015) 071301, https://doi.org/10.7567/JJAP.54.071301.

[52] T.H. Geballe, G.W. Hull, Seebeck effect in silicon, Phys. Rev. 98 (4) (1955) 940–947, https://doi.org/10.1103/PhysRev.98.940.

[53] G. Pennelli, E. Dimaggio, A. Masci, Silicon nanowires: a breakthrough for thermoelectric applications, Materials 14 (18) (2021), https://doi.org/10.3390/ma14185305, https://www.mdpi.com/1996-1944/14/18/5305.

[54] P. Martin, Z. Aksamija, E. Pop, U. Ravaioli, Impact of phonon-surface roughness scattering on thermal conductivity of thin Si nanowires, Phys. Rev. Lett. 102 (2009) 125503, https://doi.org/10.1103/PhysRevLett.102.125503, https://link.aps.org/doi/10.1103/PhysRevLett.102.125503.

[55] G. Xie, Z. Ju, K. Zhou, X. Wei, Z. Guo, Y. Cai, G. Zhang, Ultra-low thermal conductivity of two-dimensional phononic crystals in the incoherent regime, npj Comput. Mater. 4 (1) (2018) 21, https://doi.org/10.1038/s41524-018-0076-9.

[56] T. Ando, A.B. Fowler, F. Stern, Electronic properties of two-dimensional systems, Rev. Mod. Phys. 54 (1982) 437–672, https://doi.org/10.1103/RevModPhys.54.437, https://link.aps.org/doi/10.1103/RevModPhys.54.437.

[57] M.T. Björk, H. Schmid, J. Knoch, H. Riel, W. Riess, Donor deactivation in silicon nanostructures, Nat. Nanotechnol. 4 (2) (2009) 103–107, https://doi.org/10.1038/nnano.2008.400.

[58] D. Klaassen, A unified mobility model for device simulation—I. Model equations and concentration dependence, Solid-State Electron. 35 (7) (1992) 953–959, https://doi.org/10.1016/0038-1101(92)90325-7, https://www.sciencedirect.com/science/article/pii/0038110192903257.

[59] D. Klaassen, A unified mobility model for device simulation—II. Temperature dependence of carrier mobility and lifetime, Solid-State Electron. 35 (7) (1992) 961–967, https://doi.org/10.1016/0038-1101(92)90326-8, https://www.sciencedirect.com/science/article/pii/0038110192903268.

[60] W.R. Thurber, R.L. Mattis, Y.M. Liu, J.J. Filliben, Resistivity-dopant density relationship for boron-doped silicon, J. Electrochem. Soc. 127 (10) (1980) 2291, https://doi.org/10.1149/1.2129394.

[61] S. Elyamny, E. Dimaggio, S. Magagna, D. Narducci, G. Pennelli, High power thermoelectric generator based on vertical silicon nanowires, Nano Lett. 20 (7) (2020) 4748–4753, https://doi.org/10.1021/acs.nanolett.0c00227, pMID: 32463681.

[62] E. Dimaggio, G. Pennelli, Potentialities of silicon nanowire forests for thermoelectric generation, Nanotechnology 29 (13) (2018) 135401, https://doi.org/10.1088/1361-6528/aaa9a2.

[63] J.M. Ziman, Electrons and Phonons: the Theory of Transport Phenomena in Solids, Oxford University Press, 2001.

[64] C.D. Landon, N.G. Hadjiconstantinou, Deviational simulation of phonon transport in graphene ribbons with ab initio scattering, J. Appl. Phys. 116 (16) (2014) 163502, https://doi.org/10.1063/1.4898090.

[65] H. Casimir, Note on the conduction of heat in crystals, Physica 5 (6) (1938) 495–500, https://doi.org/10.1016/S0031-8914(38)80162-2, https://www.sciencedirect.com/science/article/pii/S0031891438801622.

[66] W. Li, J. Carrete, N.A. Katcho, N. Mingo, ShengBTE: a solver of the Boltzmann transport equation for phonons, Comput. Phys. Commun. 185 (2014) 1747–1758, https://doi.org/10.1016/j.cpc.2014.02.015.

[67] N.H. Protik, B. Kozinsky, Electron-phonon drag enhancement of transport properties from a fully coupled ab initio Boltzmann formalism, Phys. Rev. B 102 (2020) 245202, https://doi.org/10.1103/PhysRevB.102.245202, https://link.aps.org/doi/10.1103/PhysRevB.102.245202.

[68] M. Raya-Moreno, X. Cartoixà, J. Carrete Bte-barna, An extension of almaBTE for thermal simulation of devices based on 2D materials, Comput. Phys. Commun. 281 (2022) 108504, https://doi.org/10.1016/j.cpc.2022.108504, https://www.sciencedirect.com/science/article/pii/S0010465522002235.

[69] H.-Y. Yang, Y.-L. Chen, W.-X. Zhou, G.-F. Xie, N. Xu, Ultra-low thermal conductivity of roughened silicon nanowires: role of phonon-surface bond order imperfection scattering, Chin. Phys. B 29 (8) (2020) 086502.
[70] S.M. Goodnick, D.K. Ferry, C.W. Wilmsen, Z. Liliental, D. Fathy, O.L. Krivanek, Surface roughness at the Si(100)-SiO_2 interface, Phys. Rev. B 32 (1985) 8171–8186, https://doi.org/10.1103/PhysRevB.32.8171, https://link.aps.org/doi/10.1103/PhysRevB.32.8171.
[71] P. Giannozzi, S. Baroni, N. Bonini, M. Calandra, R. Car, C. Cavazzoni, D. Ceresoli, G.L. Chiarotti, M. Cococcioni, I. Dabo, et al., Quantum espresso: a modular and open-source software project for quantum simulations of materials, J. Phys. Condens. Matter 21 (39) (2009) 395502.
[72] P. Giannozzi, O. Andreussi, T. Brumme, O. Bunau, M.B. Nardelli, M. Calandra, R. Car, C. Cavazzoni, D. Ceresoli, M. Cococcioni, et al., Advanced capabilities for materials modelling with quantum espresso, J. Phys. Condens. Matter 29 (46) (2017) 465901.
[73] D.R. Hamann, M. Schlüter, C. Chiang, Norm-conserving pseudopotentials, Phys. Rev. Lett. 43 (1979) 1494–1497, https://doi.org/10.1103/PhysRevLett.43.1494, https://link.aps.org/doi/10.1103/PhysRevLett.43.1494.
[74] J.P. Perdew, A. Zunger, Self-interaction correction to density-functional approximations for many-electron systems, Phys. Rev. B 23 (1981) 5048–5079, https://doi.org/10.1103/PhysRevB.23.5048, https://link.aps.org/doi/10.1103/PhysRevB.23.5048.
[75] D.M. Ceperley, B.J. Alder, Ground state of the electron gas by a stochastic method, Phys. Rev. Lett. 45 (1980) 566–569, https://doi.org/10.1103/PhysRevLett.45.566, https://link.aps.org/doi/10.1103/PhysRevLett.45.566.
[76] S. Poncé, E.R. Margine, C. Verdi, F. Giustino, Epw: electron–phonon coupling, transport and superconducting properties using maximally localized Wannier functions, Comput. Phys. Commun. 209 (2016) 116–133.
[77] Y. Varshni, Temperature dependence of the energy gap in semiconductors, Physica 34 (1) (1967) 149–154, https://doi.org/10.1016/0031-8914(67)90062-6, https://www.sciencedirect.com/science/article/pii/0031891467900626.
[78] P.P. Altermatt, A. Schenk, F. Geelhaar, G. Heiser, Reassessment of the intrinsic carrier density in crystalline silicon in view of band-gap narrowing, J. Appl. Phys. 93 (3) (2003) 1598–1604, https://doi.org/10.1063/1.1529297.
[79] S.-i. Tamura, Isotope scattering of dispersive phonons in Ge, Phys. Rev. B 27 (1983) 858–866, https://doi.org/10.1103/PhysRevB.27.858, https://link.aps.org/doi/10.1103/PhysRevB.27.858.